Magnetic response of cobalt nanowires with diameter below 5 nm

P. Schio,[1,2] F. Vidal,[1,3] Y. Zheng,[1,3] J. Milano,[1,3,4] E. Fonda,[5] D. Demaille,[1] B. Vodungbo,[6] J. Varalda,[7] A. J. A. de Oliveira,[2] and V. H. Etgens[1,3]

[1]*Institut des NanoSciences de Paris, UPMC Paris 06, CNRS UMR 7588, 140 rue de Lourmel, 75015 Paris, France*

[2]*Departamento de Física, UFSCar, CP 676, 13565-905 São Carlos, SP, Brazil*

[3]*Laboratoire Franco-Argentin en Nanosciences (LIFAN), France*

[4]*CNEA-CONICET and Instituto Balseiro, CAB, UNCU, R8402AGP San Carlos de Bariloche, RN, Argentina*

[5]*Synchrotron Soleil, L'Orme des Merisiers Saint-Aubin, BP 48, 91192 Gif-sur-Yvette Cedex, France*

[6]*Laboratoire d'Optique Appliquée, ENSTA Paristech, École Polytechnique, CNRS UMR 7639, F-91761 Palaiseau Cedex, France*

[7]*Departamento de Física, UFPR, CP 19044, 81531-990 Curitiba, PR, Brazil*

(Received 17 February 2010; revised manuscript received 30 August 2010; published 21 September 2010)

The structural and magnetic properties of cobalt nanowires embedded in epitaxial CeO_2 layers are investigated. Combining electron microscopy with x-ray absorption spectroscopy, we show that polycrystalline metallic Co nanowires are formed during the growth. These nanowires are oriented in average along the growth axis with a misalignment distribution, have a predominant hcp structure and a narrow distribution of diameters. Their magnetic properties are overall dominated by shape effects with an easy axis oriented along the mean direction of the wires axis. The reversal mechanism is studied in details for samples with 3 and 5 nm mean diameters. The competition between shape and magnetocrystalline anisotropies is evidenced at 3 nm diameter. Upon reduction in the lateral dimensions, the nanowires tend to behave like aligned Stoner-Wohlfarth elongated particles with effective uniaxial anisotropy resulting from this competition.

DOI: 10.1103/PhysRevB.82.094436 PACS number(s): 75.60.Jk, 81.07.Gf, 81.15.Fg

I. INTRODUCTION

Ferromagnetic (FM) nanowires (NWs) have been the subject of intense research in recent years.[1–4] Such objects could be used as fundamental units in magnetic storage devices. Also, alternating FM metals and paramagnetic ones along the NWs axis led to the successful design of nanopillar exhibiting giant magnetoresistance.[2] The most commonly used methods to fabricate such NWs consists in filling the pores of a template, made of polymers or porous alumina, with an electrodeposited FM metal.[5–7] Such growth technique leads to regular pattern of NWs with length in the micron range. However, the geometry of the pattern is intimately linked to the characteristics of the template. As the size of the pores and the mean spacing between pores vary in the same way, it is not possible to adjust independently the diameters and the spacing of the NWs. Also, most of the studies reported in the literature deal with NWs having diameter above 5 nm.[3,4]

In this paper, we report on the structural and magnetic properties of embedded cobalt nanowires fabricated using a novel bottom-up self-assembly technique. These NWs form spontaneously during pulsed-laser deposition (PLD) of Co-containing CeO_2 epitaxial films on $SrTiO_3(001)$.[8] Such a fabrication method allows us to reach very reduced diameters. In what follows, the structural and magnetic properties of two samples, labeled d_3 and d_5, are studied. These NWs assemblies have a narrow distribution of diameters, centered on 3 nm for d_3 and 5 nm for d_5.

This paper is organized as follows: after a brief description of the experimental techniques used to grow and analyze the samples, we discuss their structure in details. Then we analyze the magnetic properties of the embedded Co NWs assemblies, evidencing distinct variation in H_c as a function of T when the diameter reaches 3 nm. We show that the magnetization reversal can be explained by taking into account the competition of shape anisotropy and magnetocrystalline anisotropy.

II. EXPERIMENTAL

Cobalt-containing CeO_2 epilayers were grown on $SrTiO_3(001)$ substrates by PLD using a KrF laser (wavelength 248 nm) operating at 2 Hz. CoO and CeO_2 targets were used. The first step of the growth is the deposition of a pure CeO_2 buffer (thickness 4 nm) under 5×10^{-2} mbar oxygen at 650 °C. Such a procedure was used in order to obtain epitaxial $CeO_2/SrTiO_3(001)$ thin films, as reported previously.[9] After this first step ensuring epitaxial growth of the matrix, Co-containing CeO_2 was grown at a pressure lower than 10^{-5} mbar. For the growth of 5 nm diameter nanowires, the temperature was 650 °C. Reducing the growth temperature led to a reduction in the NWs diameter down to 3 nm. This issue will be detailed in a separate publication. Tuning the ratio of laser shots on the CoO and CeO_2 targets enabled us to adjust the Co content in the epilayers. The real Co content was determined by Rutherford backscattering calibration as ~85% of the nominal content given by the percentage of laser shots on the cobalt containing target. The same 12.5% Co content was used for the d_3 and d_5 samples.

X-ray reflectivity measurements were carried out in order to evaluate the quality of the films. The measured rugosity was 0.3 nm and no porosity was detected. The density of the epilayers was the same as that of CeO_2. High-resolution transmission electron microscopy (HRTEM) and energy-filtered TEM (EFTEM) data were acquired using a JEOL JEM 2100F equipped with a field-emission gun operated at 200 kV and a Gatan GIF spectrometer.

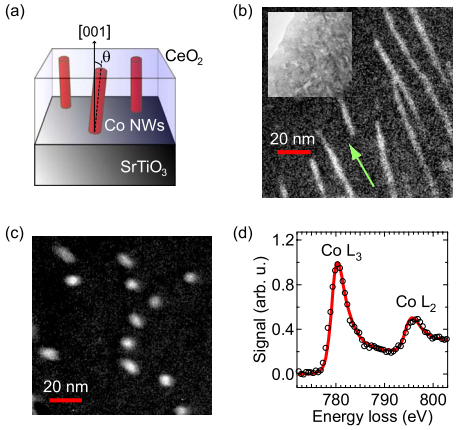

FIG. 1. (Color online) (a) Scheme of the structure of epilayers containing embedded cobalt NWs. θ is the misalignment of the wires defined as the absolute value of the angle between the wire axis and the growth direction [001]. (b) Typical EFTEM cross section showing aggregation of cobalt in thin wires with long axis running along directions slightly misaligned with respect to the growth direction (indicated by an arrow). Inset: zero loss image. (c) Typical plane-view EFTEM image. (d) EELS spectrum at cobalt L edge of a sample containing NWs (○) and of a reference cobalt sample (thick line).

Magnetic measurements were performed in a superconducting quantum interference device magnetometer [Magnetic Property Measurement System (MPMS) 5S Quantum Design]. The data were corrected by removing the high-field slope related to the diamagnetic contribution of the substrate.

X-ray absorption near-edge spectroscopy (XANES) and extended x-ray absorption fine structure (EXAFS) data (in the Co K-edge spectral range) were collected on the SAMBA beamline of Synchrotron SOLEIL (St. Aubin, France). The beamline uses two Pd-coated mirrors for collimating the white beam on the monochromator and focusing the monochromatic beam down to the sample. The sagittally focusing monochromator used was a Si 220 fully tuned while mirrors were used to reject the harmonics. Dynamic sagittal focusing was used in order to keep the beam size constant over a scan. The impinging x-ray intensity was monitored by an ionization chamber containing a mixture of nitrogen and helium and the K fluorescence intensity by a silicon drift detector. Opting for fluorescence detection allowed us to probe the whole epilayers. The main experimental difficulty was due to the fluorescence of the ceria matrix that is quite close to that of cobalt, therefore an aluminum foil was used to reduce the contribution of the lower energy lines. Nonetheless, the cobalt fluorescence was still a small contribution. XANES data analysis was performed with theoretical standards calculated with FEFF 8.4 (Ref. 10) and EXAFS data analysis with the IFEFFIT package.[11]

III. STRUCTURE OF NANOWIRES

A. Transmission electron microscopy

Co segregation occurs during the growth of doped CeO_2 epilayers, resulting in an assembly of NWs, as sketched in Fig. 1(a). We define θ, the misalignment of the wires as the absolute value of the angle between the long axis of a wire and the growth direction that corresponds to the [001] direction of the $SrTiO_3$ substrate.

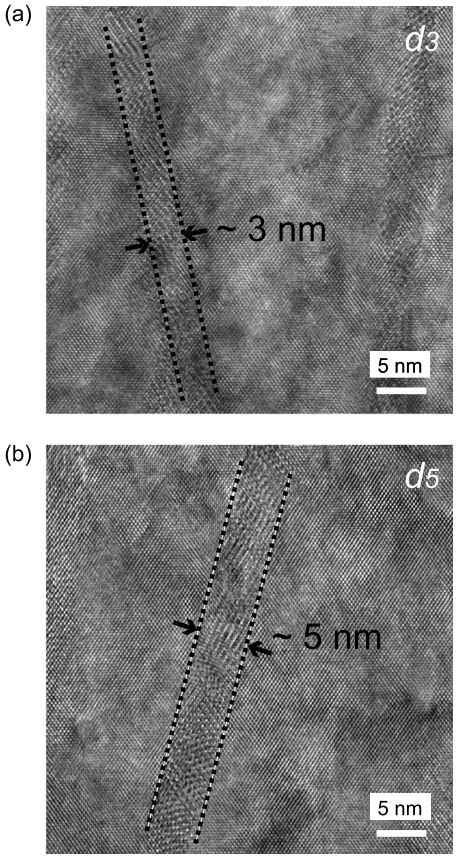

FIG. 2. HRTEM cross section showing Co NWs within the CeO_2 matrix for samples with NWs of different diameters: (a) sample d_3 with 3 nm and (b) sample d_5 with 5 nm.

The formation of NWs, with length in the 100 nm range, is evidenced by EFTEM images, taken at Co L edge, in cross section and plane views [Figs. 1(b) and 1(c)]. As evidenced in Fig. 1(b), the NWs are not perfectly aligned on the growth direction, most of them grow in directions deviating slightly from [001]. The shapes of the spot corresponding to wires in the EFTEM plane view are not identical: some are circular while others are elliptic. This is due to the orientation distribution: a wire oriented along the growth direction will be seen as a circular spot in the plane view and a slanted wire will appear as an elliptic spot.

Filtered images allow us to map the Co location. In order to determine the valence state of Co in the wires, we also performed electron-energy-loss spectroscopy (EELS) during TEM experiments. The EELS spectra of NWs containing samples and reference Co metal are quite similar at Co L edge, indicating that the NWs are made of metallic cobalt [Fig. 1(d)].

HRTEM cross-section views of the embedded NWs are displayed in Figs. 2(a) and 2(b), evidencing NWs with different diameters. We note that due to (i) the misorientation of the grains in NWs with respect to the epitaxial CeO_2 layer and (ii) multiple electron scattering, it is quite difficult to

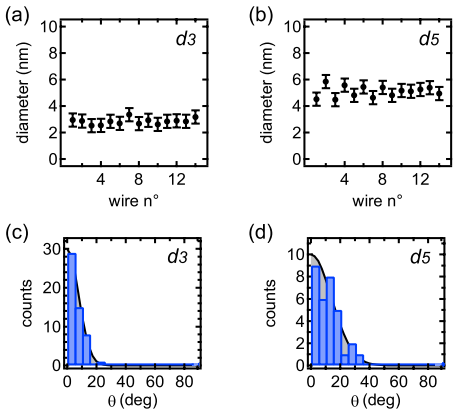

FIG. 3. (Color online) [(a) and (b)] NWs diameters measured in different zones of sample d_3 and d_5, respectively. [(c) and (d)] Misalignment distribution for sample d_3 and d_5, respectively.

derive information on the grain size and orientation distributions from TEM cross sections. This issue deserves further investigation and is currently being explored in detail.

Figures 3(a) and 3(b) show measurements, performed on EFTEM images, of the wire's diameters in sample d_3 and d_5, respectively. Since the error bar in these measurements and the dispersion of the values are of the same order of magnitude, we do not present the results in the form of histograms. Such diameter measurements were repeated in different zones of d_3 and d_5 and indicate narrow distributions centered on mean diameters of 3 and 5 nm for d_3 and d_5, respectively.

The misalignment distributions in samples d_3 and d_5 are given in Figs. 3(c) and 3(d), respectively. From the widths of the distribution, it is evident that the wires are better oriented in sample d_3 than in sample d_5.

B. X-ray absorption spectroscopy at Co *K* edge

Having established the formation of metallic cobalt nanowires within the samples, we now examine their structure in a more detailed way. Indeed the determination of the crystalline structure of Co is important because it is intimately linked to the magnetic properties. Cobalt is usually found to crystallize in a hcp structure at room temperature and ambient pressure. However, above 425 °C a phase transition occurs leading to the transformation in a fcc structure. It is not uncommon to find fcc Co embedded clusters in composite samples because of a quenching of the fcc-hcp transition during the cooling phase following growth as in the case of Co clusters in Ag.[12] Contrary to fcc Co, hcp Co has a strong uniaxial magnetocrystalline anisotropy, directed along the *c* axis, $K_{1,u}$. At low temperature, $K_{1,u}=7.6\times10^5$ J m^{-3}, of the same order of magnitude as the shape anisotropy, K_S, obtained when considering an infinitely long Co wire: $K_S=(\mu_0/4)M_s^2=6.6\times10^5$ J m^{-3} (M_s is the saturation magnetization). As both energies fall in the same range, it is important to determine whether Co exists under the fcc or hcp structure within the embedded NWs.

To address this issue, we have used x-ray absorption spectroscopy. Before presenting the results, we note that x-ray diffraction studies did not allow us to detect cobalt in our samples, indicating a polycrystalline state. We present in what follows x-ray absorption data recorded at the Co *K* edge on the d_3 sample and a hcp Co foil reference sample.

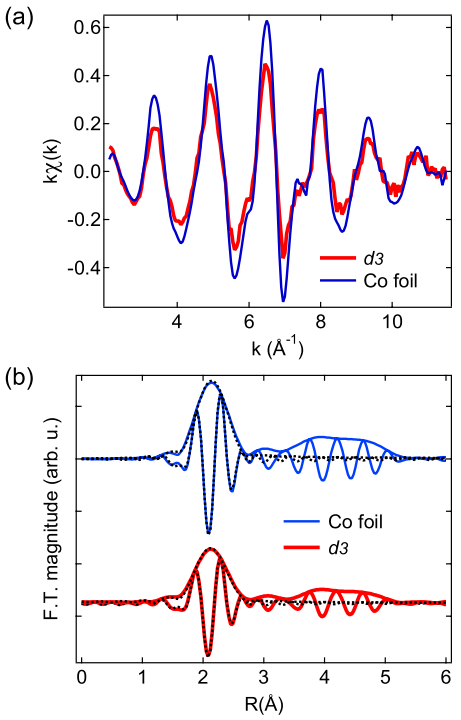

FIG. 4. (Color online) (a) *k*-weighted EXAFS spectra of d_3 (thick gray line) and of a Co foil (thin gray line). (b) Fitted EXAFS Fourier transforms obtained for d_3 (thick gray line) and the reference sample (thin gray line) at the Co *K* edge. Dashed lines are fits.

These data can be observed from two points of view: EXAFS and XANES. In the EXAFS part, the analysis is quite straightforward, the oscillations of the sample and reference match very well as shown in Fig. 4(a), and the signal was simulated by a Co single shell surrounding the Co absorber, Fig. 4(b). Oxygen is not detected as shown by the absence of Co-O related peak in the Fourier-transformed signal. This proves that most of Co atoms have not entered the CeO_2 structure. At the same time, the Co-Co coordination number is quite low and it could be ascribed to the small size of the Co segregate. If we suppose that Co is in the form of spherical particles we can use a simple formula to obtain the mean particle diameters given in Table I: $N=12(1-\frac{3R}{2D})$, where N is the coordination number, R the interatomic dis-

TABLE I. Parameters deduced from fitting the EXAFS and XANES data for a reference sample (metallic Co foil) and d_3. N: coordination number, R: interatomic distance, E_e: edge shift, and D: deduced grain diameter.

	N	R (Å)	E_e (eV)	% Co[a]	D (nm)
Foil	12.5	2.488(6)	−1(1)	100	
d_3	8.9(7)	2.486(5)	−1(1)	99(1)	1.6(4)

[a]Co hcp percentage as evaluated by comparing the XANES spectra of the samples to the reference spectrum of hcp cobalt.

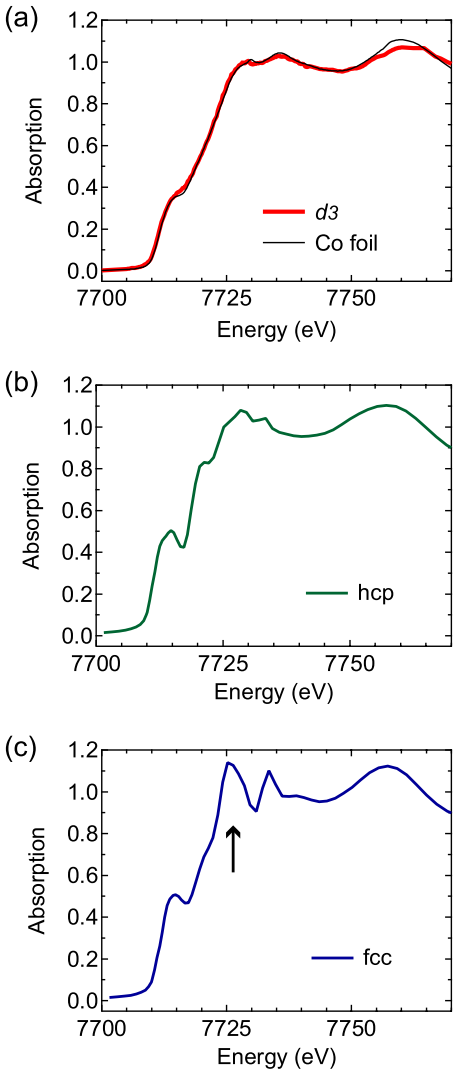

FIG. 5. (Color online) (a) Co *K*-edge XANES spectra obtained for d_3. The thin black line is the reference spectrum obtained from a Co foil. [(b) and (c)] Calculated spectra for (b) hcp and (c) fcc Co.

tance, and D is the particle diameter.[13] The use of this formula and the assumption of spherical particles is certainly a crude approximation but it nevertheless gives a rough estimate—or lower value—of the dimensions of the grains constituting the NWs, confirming their polycrystalline character.

As shown in Fig. 5(a), the XANES spectrum of d_3 matches that of an hcp Co foil quite well. The effect of the fcc/hcp phase transition is not much visible in the EXAFS especially if it is not possible to analyze an epitaxial growth and take advantage of x-ray polarization to undercover the anisotropy of hcp with respect to fcc. In our case all signals are isotropic under all angles with respect to sample surface (data not shown). But in the XANES region the difference between hcp and fcc is much more evident, even for disordered or statistically oriented systems and it is due to the difference in the arrangement of multiple-scattering paths. This is illustrated in Figs. 5(b) and 5(c) where two *ab initio* calculated XANES spectra for hcp and fcc structures are depicted, the peak marked by an arrow is much more pronounced in the fcc form than in the hcp in agreement with other studies.[12] Comparing such simulated spectra with the one obtained on NWs and on the reference, we deduce that Co crystallizes mainly in the hcp arrangement with possible minority fcc regions that cannot be completely excluded. The results from XANES and EXAFS analysis are summarized in Table I.

C. Summary of TEM and XAS results

From what precedes, we can deduce the following information about the structure of the NWs in d_3 and d_5: (i) the NWs are oriented in average along the growth axis with a misalignment distribution (this distribution is more narrow for d_3 than for d_5); (ii) they are made of metallic Co; (iii) d_3 and d_5 have diameter narrow distributions centered on 3 nm and 5 nm, respectively; and (iv) they have a polycrystalline structure with a vast majority of hcp grains and possible trace of fcc ones.

IV. MAGNETIC RESPONSE

A. Hysteresis loops of d_3 and d_5

Figure 6 shows the hysteresis loops, taken at different temperatures, with the applied field perpendicular (out of plane, OP) and parallel (in plane, IP) with respect to the surface of samples [(a) and (b)] d_3 and [(c) and (d)] d_5. The measurement geometry is depicted in Fig. 6(e). The squareness of the loops, defined as the ratio of remanence and saturation magnetization (M_r/M_s), is given in Table II. For both samples, the hysteresis loops have higher squareness in the OP direction, i.e., along the mean value of θ. This corresponds to the usual behavior observed in oriented magnetic wires assemblies with low dipolar interactions between wires and indicates that the magnetic anisotropy is overall dominated by shape anisotropy with an easy axis along the $\theta=0$ direction.

Although it is clear that the easy axis is along the growth direction and that the (001) plane of the $SrTiO_3$ substrate is a hard plane, the shape of the hysteresis loops deviates somewhat from the ideal case (corresponding to a perfectly square OP loop and a linear, closed, IP loop). For d_3 and d_5, sheared loops with a trapezoidal shape are observed in the OP direction. There is obviously a switching field distribution that can be obtained by taking the derivative of the magnetization with respect to the applied field. The mean value of the switching field $\mu_0 H_{sw}$ and width $\mu_0 \Delta H_{sw}$ of the distribution can be extracted from a Gaussian fitting of $dM/d\mu_0 H$, as shown in Fig. 6(f). The results of this analysis are listed in Table II.

The origin of the OP loops shape and switching field distribution can lie in: (i) misalignment of wires with respect to the OP direction, (ii) dipolar interactions between wires, and (iii) inhomogeneities, with some wires having switching fields deviating from the mean value. The last effect is intimately connected with the structural quality of the wires: defects can act as nucleation centers and lead to early flipping of wires while increased crystalline quality generally results in enhanced value of the switching field.

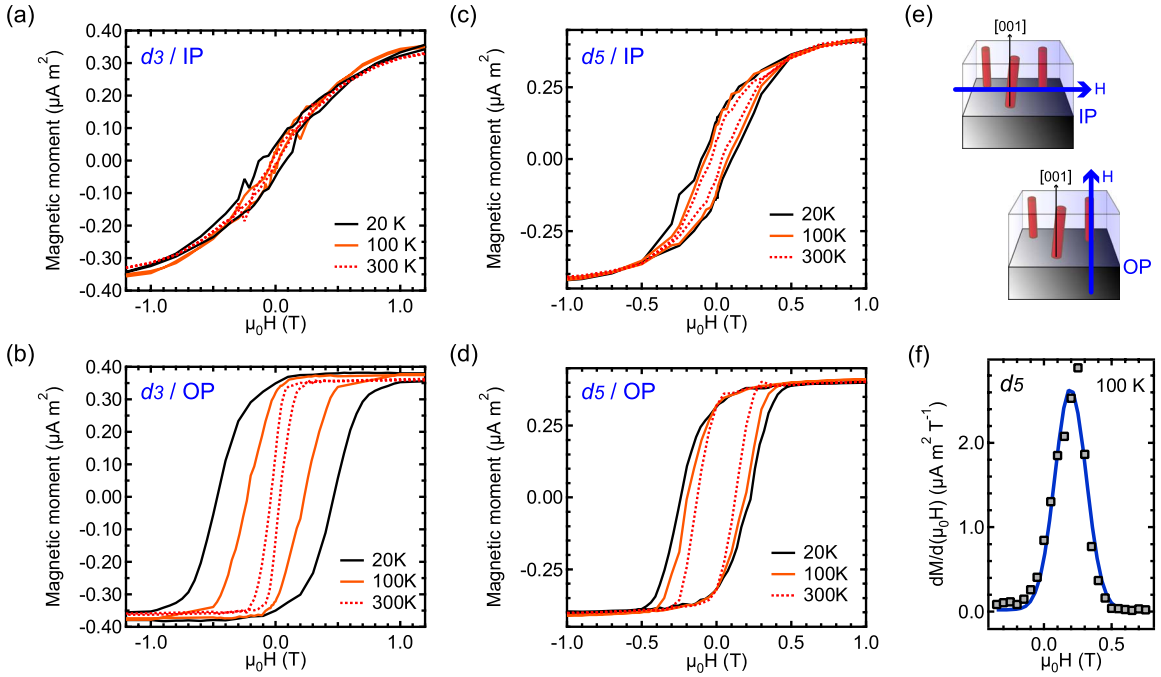

FIG. 6. (Color online) Magnetic response of the d_3 NW assembly. Hysteresis curves for field applied (a) parallel, IP, and (b) perpendicular, OP, to the film plane at different temperatures. [(c) and (d)] Same as (a) and (b) but for the d_5 NW assembly. Black lines: cycles measured at $T=20$ K, gray lines $T=100$ K, dashed lines $T=300$ K. (e) Schemes of the IP and OP configuration. (f) OP switching field distribution of d_5 at $T=100$ K (squares) with Gaussian fit (line).

A broad misalignment distribution has also an impact on hysteresis loops in the hard direction, causing an opening of the cycles. The IP cycles of d_5 show a strong opening while those of d_3 are quite closed with very low squareness. This can be rationalized by taking into account the orientation distributions of d_3 and d_5. A substantial ratio of wires have a strong misalignment in d_5, this lies at the origin of the observed opening of the IP loops in this sample. Indeed the squareness in the IP direction is clearly correlated with the width of the orientation distribution of the wires for d_3 and d_5.

Strong dipolar interactions between wires can cause an inversion of easy axis in NW ferromagnetic assemblies with the axis of wires becoming a hard axis when these interactions become dominant. This has indeed been observed in assemblies with high density and very long wires (micron length and over).[14] In the present case, the easy axis of d_3 and d_5 remains oriented along the average direction of the wires axis. This indicates that the shape effect is still the dominating term when compared to the magnetostatic coupling between wires.

Contrary to the effect of misorientation and dipolar interactions, the effect of structural inhomogeneities on the loops shape and switching field distribution can depend sensitively on the temperature. Fluctuation of the crystalline orientation along the wires axis and among wires can result in an inhomogeneous distribution of magnetic anisotropy energy through temperature-dependent terms linked to the magnetocrystalline anisotropy. In the case of d_5, $\mu_0\Delta H_{sw}$ exhibit a small drop with increasing temperature, indicating limited effects related to the crystalline texture. This is not the case of d_3 for which a sharp drop of $\mu_0\Delta H_{sw}$ is observed at 300 K, falling from 0.38 to 0.17 T. This could indicate that the internal crystalline structure of wires in d_3 have a substantial impact on the magnetic response. We will discuss this point further in the following sections devoted to the magnetization reversal mechanism in d_3 and d_5.

TABLE II. Summary of magnetic data for d_5 and d_3 samples.

Sample	T (K)	Squareness, OP	Squareness, IP	$\mu_0 H_{sw}$ (T), OP	$\mu_0\Delta H_{sw}$ (T), OP
d_5	20	0.80	0.31	0.238	0.285 ± 0.010
d_5	100	0.79	0.29	0.195	0.271 ± 0.010
d_5	300	0.80	0.15	0.131	0.210 ± 0.005
d_3	20	0.92	0.13	0.468	0.375 ± 0.011
d_3	100	0.84	0.08	0.224	0.386 ± 0.016
d_3	300	0.36	0.04	0.030	0.173 ± 0.007

B. Coercive field and magnetization reversal

1. Reversal mechanism in ferromagnetic nanowires

We begin this section by a short glimpse on the magnetization reversal mechanism in nanowires. Our purpose is not to give an extensive review of the field here, for complete reviews we refer the reader to Refs. 3 and 4. Due to their high aspect ratio, the magnetic properties of ferromagnetic nanowires are dominated by shape anisotropy.[4] The fundamental issue of the magnetization reversal mechanism of these objects has been much studied recently.[15–22] Considering a perfect nanowire, it can be shown theoretically that a transition between reversal via curling mode at high diameter d and coherent uniform rotation occurs when d falls below a critical value $d_{crit}=\sqrt{24A/\mu_0 M_s^2}$, where A is the exchange stiffness.[23–25] This reversal mode through coherent rotation is *delocalized*: it extends throughout the whole wire.

Experimental studies performed on NWs assemblies as a function of the diameter have confirmed the occurrence of a transition when $d<d_{crit}$.[19] Below this critical value, the dependence of the coercivity on the temperature could be fitted quite satisfactorily using equations derived in the framework of thermally activated reversal through coherent rotation. However, the results deviates from the Stoner-Wohlfarth model of uniform *delocalized* coherent rotation reversal:[26] the activation volume is found to be two order of magnitude lower that the physical volume of the NWs and the coercive field at low temperature is roughly one third of the predicted value (i.e., the anisotropy field). Studies performed on individual NWs also evidenced that the reversal is a localized process.[27] These results can be rationalized by taking into account the defective structure of the wires giving rise to localization effects. The reversal occurs via a coherent mechanism in *localized* regions with reduced dimensions as compared to the physical size of the NWs.

2. Contributions to the magnetic anisotropy energy of ferromagnetic Co nanowires assemblies

The main contribution to the anisotropy is the shape anisotropy, given by $K_S=(\mu_0/4)M_s^2$. In the case of cobalt, $K_S=6.6\times10^5$ J m^{-3}. Another magnetostatic contribution is related to the dipolar interactions between wires. In the case of a regular array of NWs, it can be shown that dipolar coupling leads to a contribution $K_{dip}=-3.15(\mu_0/4)M_s^2\rho^2L/\delta$, where L is the length of the wires, ρ is the radius of wires, and δ the mean distance between neighboring wires.[14] We note that in the present case this simple formula may overestimate the dipolar interactions because the d_3 and d_5 NWs assemblies are not ordered in the plane and there is some orientation distribution. K_S and K_{dip} have the same dependence with respect to M_s and can be merged in a single contribution as $K_m=K_S+K_{dip}=(\mu_0/4)M_s^2(1-3.15\rho^2L/\delta)$. From this expression, it is obvious that strong dipolar coupling (for large L and small δ) can induce a switching of the easy axis into a hard one (if $K_m<0$). In the present case, the magnetostatic contribution K_m is positive and is overall still dominated by shape effects since the easy axis is oriented along the average axis direction of the NWs assemblies. Indeed, taking L as half the thickness of the films and using δ values obtained for d_3 and d_5 gives a $|K_{dip}|/K_S$ ratio on the order of 20–30 %. A more precise estimate would require to take into account the orientation distribution and the effect of in-plane disorder. To conclude with the magnetostatic anisotropy, an important point is that it does not depend on the temperature in the range where M_s is constant.

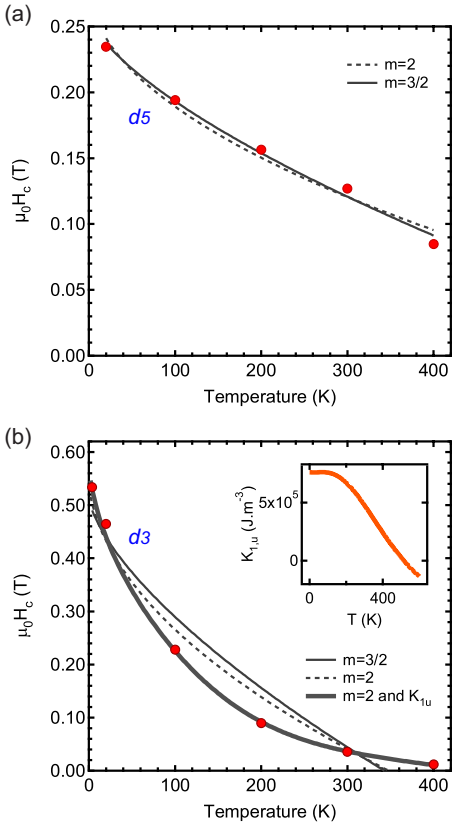

FIG. 7. (Color online) Coercive field (OP) as a function of temperature (gray ○) and fits to Eq. (4) for (a) d_5 sample and (b) d_3 sample. The temperature dependence of $K_{1,u}$ is given in the inset of (b), adapted from Ref. 28.

Contrary to the previous contributions, the magnetocrystalline anisotropy may depend strongly on the temperature.[28] $K_{1,u}$, the uniaxial magnetocrystalline anisotropy of hcp Co, is roughly constant below 200 K and decreases beyond this limit, as shown in the inset of Fig. 7(b). Depending on the crystalline orientation of hcp Co within the wires, this term can enhance the total anisotropy or compete with the magnetostatic term: if the c axis of cobalt is along the wire axis, then both contributions add; if the c axis lies perpendicular to the wire axis, then $K_{1,u}$ plays against the magnetostatic term.

3. $H_c(T)$ law for thermally activated reversal through coherent rotation

Considering the fact that $d_{crit}=15$ nm for Co, we will analyze the reversal mechanism in d_3 and d_5 in the framework of coherent rotation.

In cases where the magnetic anisotropy is dominated by the contribution arising from the shape, the variation in the coercive field with temperature can be modeled as[19]

TABLE III. Parameters deduced from fitting the $H_c(T)$ data for d_5 and d_3 samples.

	$\mu_0 H_{c,0}$ (T)	E_0 (eV)	m	$V^\star$ (nm^3)	η (nm^3)	ℓ (nm)
d_5	0.26	1.6	1.5	700	0	30
d_3	0.63	1.1	2	190	110	27

$$H_c(T) = H_{c,0}\frac{M_s(T)}{M_{s,0}}\left\{1 - \left[\frac{25k_BTM_{s,0}^2}{E_0M_s^2(T)}\right]^{1/m}\right\}, \quad (1)$$

where $H_{c,0}$ is the coercive field at 0 K, E_0 the energy barrier for reversal, related to shape anisotropy, $M_s(T)$ and $M_{s,0}$ the saturation magnetization at temperature T and 0 K, respectively. The value of m is in general equal to $\frac{3}{2}$. In the special case of aligned Stoner-Wohlfarth particles, $m=2$.

As dipolar and shape contribution have the same $M_s^2(T)$ dependence, including the effect of dipolar coupling can still be modeled in the same way. E_0 simply results from the balance of these two terms. Neglecting the variation in the saturation magnetization [$M_s(T)$ is roughly constant in the temperature range studied], we have

$$H_c(T) = H_{c,0}\left[1 - \left(\frac{25k_BT}{E_0}\right)^{1/m}\right]. \quad (2)$$

We also take into account the influence of the magnetocrystalline anisotropy, limiting our analysis to the effect of the leading term, $K_{1,u}$. This is indeed justified by the results of the structural analysis showing that Co crystallizes in the hcp structure. Including the effect of magnetocrystalline anisotropy, we can write the energy barrier as

$$E^\star \simeq E_0 - \eta K_{1,u}, \quad (3)$$

where η scales as a volume. The sign of the $K_{1,u}$ contribution reflects the assumption of an orientation of the c axis of hcp Co leading to a competition between magnetostatic and magnetocrystalline contributions. The coercive field can then be fitted using

$$H_c(T) = H_{c,0}\left[1 - \left(\frac{25k_BT}{E^\star}\right)^{1/m}\right]. \quad (4)$$

4. Variation in H_c with the temperature in d_3 and d_5

Comparison of the magnetic behavior of the two samples reveals two striking differences: (i) at low temperature, the coercive field, H_c, in the OP direction is much lower for the d_5 sample ($\sim$0.2 T) than for d_3($\sim$0.5 T); (ii) while H_c decreases slowly with increasing temperatures for NWs of 5 nm diameter, it drops sharply for NWs of 3 nm. This is best seen in Fig. 7 where H_c is plotted as a function of the temperature for the two diameters.

The evolution of the coercive field with T has been fitted using Eq. (4) for both samples. Considering d_5, fitting $H_c(T)$ gives satisfactory results with $\eta=0$: the evolution of the coercive field is quite well reproduced both for $m=\frac{3}{2}$ and $m=2$, as shown in Fig. 7(a). Both exponents lead to roughly the same values of $H_{c,0}$ and E_0:E_0=1.6 eV (1.9 eV), $\mu_0 H_{c,0}$=0.26 T (0.28 T) for $m=\frac{3}{2}$($m=2$). The good agreement indicates clearly that the evolution of H_c can be reproduced by considering a temperature-independent energy barrier related to K_m. The values obtained for E_0 and $H_{c,0}$ are also in quite good agreement with previous measurements by Zeng *et al.*[19] for NWs with diameter below d_{crit}=15 nm down to 5.5 nm ($E_0 \simeq 3$ eV for 5.5 nm diameter and $\mu_0 H_{c,0}$=0.32 T, roughly one third of the anisotropy field). The major difference in our case lies in the fact that both $m=\frac{3}{2}$ and $m=2$ power laws fit the data in contrast to the clear failure of the quadratic law reported previously.

Reducing the NWs diameter reveals a change in the evolution of H_c with temperature. For the 3 nm diameter NWs, using Eq. (4) with $\eta=0$ does not allow us to fit properly the temperature dependence of H_c, neither for $m=2$ nor for $m=\frac{3}{2}$. The assumption of a temperature-independent barrier clearly fails. It is then necessary to call for other source of anisotropy as taking into account shape anisotropy only is not sufficient to reproduce the data.

As seen in Fig. 7(b), fitting the data with a $K_{1,u}$-related contribution gives quite good results. For $m=2$ [thick line in Fig. 7(b)], we obtain $E_0=1.1\pm0.1$ eV, $\mu_0 H_{c,0}$=0.63 T, and η=110 nm^3. As $E_0 > \eta K_{1,u}$, K_m is still the leading term in the magnetic anisotropy. Fitting the data with $m=\frac{3}{2}$ gives similar values of the parameters.

From $E_0=\mu_0 H_{c,0} M_{s,0} V^\star$, we deduce $V^\star$, the effective volume for activation of the reversal mechanism: $V^\star$=190 nm^3. This indicates that the magnetization does not reverse coherently in the whole NW. The reversal is localized in regions of volume $V^\star$. This volume corresponds to cylindrical sections having the same diameter $d=3$ nm as the NWs and a length $\ell \sim 27$ nm, i.e., rods with an aspect ratio $\ell/d=9$. The parameters derived from the fitting procedure are summarized in Table III.

The fact that $\eta K_{1,u}$ reduces the value of $E^\star$ indicates that the misorientation of the hcp grains in the NWs is not random and that, furthermore, the c axis is oriented in average (over the localization volume) in a direction lying closer to the plane of the substrate than to the axis of the wires. This leads to an effective contribution of $K_{1,u}$ that tends to decrease the energy barrier imposed by the shape anisotropy in the plane perpendicular to the NWs axis. The magnetocrystalline anisotropy plays against the shape anisotropy. According to this interpretation, the competition between $K_{1,u}$ and K_m is important at low temperatures in the interval where $K_{1,u}$ takes high values and is roughly constant. The effects are less pronounced above $\sim$200 K, where $K_{1,u}$ drops while the shape anisotropy remains constant. This is in line with the observed sharp drop of $\mu_0 \Delta H_{sw}$ between 100 and 300 K discussed in the previous section. Indeed the existence of a distribution of grains with different sizes and orientation of

the c axis may result in a broad distribution of local effective anisotropy. This would result in a broad switching field distribution in the temperature range where $K_{1,u}$ is large, as observed (Table II).

From $V^\star$ and $E^\star$ it is then possible to extract an effective anisotropy $K^\star$, resulting from the competition between magnetocrystalline and shape anisotropies, given by

$$K^\star = E^\star / V^\star. \tag{5}$$

From this equation, we deduce $K^\star = 4.5 \times 10^5$ J m^{-3} at low temperature. This value allows us to estimate the anisotropy field H_a at zero temperature, given by

$$\mu_0 H_a = \frac{2K^\star}{M_{s,0}}. \tag{6}$$

We get $\mu_0 H_a = 0.62$ T. This value matches quite well the value of the coercive field at low temperature, $\mu_0 H_{c,0} = 0.63$ T. The coercive field at low T approaches the value predicted for rotation in unison. The fact that $H_a = H_{c,0}$ combined with the fit to a quadratic law of $H_c(T)$ are strong indications in favor of a localized reversal mode following the Stoner-Wohlfarth model. Globally, the above analysis supports the idea that magnetization reversal in the 3 nm diameter NWs occurs through a coherent rotation in localized sections of ~27 nm length.

Having discussed the case of 3 nm diameter NWs in details, we come back to the 5 nm case and the question that arises naturally is the following: how to council these results with the fact that $\eta = 0$ works well in the case of 5 nm diameter NWs? Concerning d_5, the values of H_c and its variation with temperature are analogous to those reported previously for polycrystalline Co nanowires grown by electrodeposition.[19] The magnetic behavior of such samples could be described by invoking shape anisotropy only. We put forward the hypothesis that the polycrystalline character of the wires, more precisely, the reduced grain sizes and the grain orientation distribution, may be responsible for the absence of $K_{1,u}$-related contribution in d_5. In regions with typical size below the exchange length, the magnetic moments are aligned in order to minimize the exchange energy. The magnetocrystalline anisotropy contribution is then averaged by exchange. This latter contribution can be averaged out as the grain size and fraction of well-crystallized matter (inside the grains, as opposed to disorder in grain boundaries) tend toward zero. Such effect has been thoroughly studied previously in the framework of random anisotropy description of polycrystalline magnets.[29] In the case of very small grains with multiple orientations, as illustrated schematically in Fig. 8(a), the contribution of $K_{1,u}$ will tend to vanish, leaving K_m as the only source of magnetic anisotropy. Alternatively, in the case of grains with lateral dimensions equal to the wire's diameter, the contribution of $K_{1,u}$ is not averaged out effectively [Fig. 8(b)].

We note that in this range of diameters, the magnetic properties depend strongly on the crystalline quality of the wires, more precisely on the size of the grains. As a consequence, finding ways to enhance the crystalline quality of embedded Co wires is a prerequisite to further study on the magnetization reversal and dynamics in such objects. A recent study on chemically prepared nanorods showed that H_c can reach high values in single crystalline elongated objects with a well defined and proper orientation of Co c axis.[30]

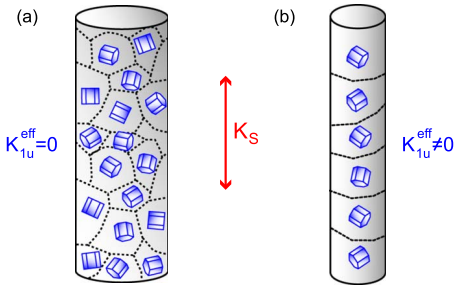

FIG. 8. (Color online) Schemes of polycrystalline NWs with local orientation of the grains leading to (a) an effective averaging of $K_{1,u}$ and (b) a contribution of $K_{1,u}$ to the total magnetic anisotropy energy. The local magnetocrystalline anisotropy axis is the c axis of the hexagonal unit cell. The shape anisotropy axis is indicated by the double arrow.

Another possible explanation for the distinct behavior of 3 nm and 5 nm diameter NWs would be the influence of a possible temperature-dependent term related to surface anisotropy. Indeed, in the present case, the surface/volume ratio evolves as $1/\rho$ with ρ the radius of the NWs. Therefore, one expects a more pronounced influence of the surface term, if present, in the case of lower diameters. More precisely, the surface/volume ratio should be 5/3 times larger in the case of 3 nm diameters NWs than for 5 nm diameter NWs. This ratio is rather low and we are thus left with the natural conclusion that a surface-related contribution may not explain the strikingly dissimilar behavior observed. However, further studies on the effect of size reduction will be necessary in order to track a possible surface effect. We are currently exploring ways to reduce the diameter of the wires below 3 nm.

V. CONCLUSION

Polycrystalline hcp Co NWs assemblies, labeled d_3 and d_5 have been produced by pulsed laser deposition. The wires are embedded in an epitaxial CeO_2 matrix and oriented along the growth direction. Their mean diameter is very small, 3 nm for d_3 and 5 nm for d_5, and the diameter distribution is narrow.

The magnetic reversal mechanism has been studied in details for d_3 and d_5, revealing distinct behavior. The anisotropy of wires with 5 nm diameter is dominated by the shape contribution and the reversal is localized. As the diameter decreases to reach 3 nm, the reversal cannot be described by a temperature-independent energy barrier. In this case, competition between magnetocrystalline and shape anisotropy leads to an effective temperature-dependent anisotropy, $K^\star$. The reversal can be described by the Stoner-Wohlfarth model applied to a chain of elongated particles (diameter 3 nm, length $\simeq$ 27 nm) with uniaxial anisotropy $K^\star$.

To conclude, the self-assembly of embedded NWs might be a way to produce even smaller NWs by a careful control of growth parameters. The growth mechanism of these ob-

jects clearly deserves further investigation as its comprehension is of strategic importance in order to master and possibly steer the self-assembly of NWs.

ACKNOWLEDGMENTS

The authors gratefully thank L. Steren and M. Marangolo for stimulating discussions, B. Capelle and E. Larquet, IMPMC, CNRS-UPMC, for access to the TEM facilities and acknowledge financial support from ECOS-Sud and French-Brazilian CAPES-COFECUB under Program No. 560/2007. We are also grateful to Region Ile-de-France for convention SESAME 2000 E1435 for the support to cryoelectron microscope JEOL 2100F installed at IMPMC UMR 7590. P.S. acknowledges support from FAPESP (Grants No. 2007/08649-5 and No. 2008/10276-5).

[1] R. Skomski, J. Phys.: Condens. Matter **15**, R841 (2003).
[2] A. Fert and L. Piraux, J. Magn. Magn. Mater. **200**, 338 (1999).
[3] D. J. Sellmyer, M. Zheng, and R. Skomski, J. Phys.: Condens. Matter **13**, R433 (2001).
[4] L. Sun, Y. Hao, C.-L. Chien, and P. C. Searson, IBM J. Res. Dev. **49**, 79 (2005).
[5] J. C. Lodder and L. Cheng-Zhang, IEEE Trans. Magn. **25**, 4171 (1989).
[6] H. Masuda, H. Yamada, M. Satoh, and H. Asoh, Appl. Phys. Lett. **71**, 2770 (1997).
[7] S. Sun, C. B. Murray, D. Weller, L. Folks, and A. Moser, Science **287**, 1989 (2000).
[8] F. Vidal, Y. Zheng, J. Milano, D. Demaille, P. Schio, E. Fonda, and B. Vodungbo, Appl. Phys. Lett. **95**, 152510 (2009).
[9] Y. Zheng, B. Vodungbo, F. Vidal, M. Selmane, and D. Demaille, J. Cryst. Growth **310**, 3380 (2008).
[10] A. L. Ankudinov, B. Ravel, J. J. Rehr, and S. D. Conradson, Phys. Rev. B **58**, 7565 (1998).
[11] M. Newville, J. Synchrotron Radiat. **8**, 322 (2001).
[12] G. Zhang, Z. Y. Wu, A. Li, Y. Wang, J. Zhang, M. I. Abbas, R. Hu, X. Ni, Y. Tong, and Y. Hwu, Phys. Rev. B **69**, 115405 (2004); J. Miyawaki, D. Matsumura, A. Nojima, T. Yokoyama, and T. Ohta, Surf. Sci. **601**, 95 (2007).
[13] M. Borowski, J. Phys. IV **7**, C2-259 (1997).
[14] G. J. Strijkers, J. H. J. Dalderop, M. A. A. Broeksteeg, H. J. M. Swagten, and W. J. M. de Jonge, J. Appl. Phys. **86**, 5141 (1999).
[15] M. E. Schabes, J. Magn. Magn. Mater. **95**, 249 (1991).
[16] P. M. Paulus, F. Luis, M. Kröll, G. Schmid, and L. J. de Jongh, J. Magn. Magn. Mater. **224**, 180 (2001).
[17] R. Skomski, H. Zeng, M. Zheng, and D. J. Sellmyer, Phys. Rev. B **62**, 3900 (2000).
[18] R. Skomski, H. Zeng, and D. J. Sellmyer, J. Magn. Magn. Mater. **249**, 175 (2002).
[19] H. Zeng, R. Skomski, L. Menon, Y. Liu, S. Bandyopadhyay, and D. J. Sellmyer, Phys. Rev. B **65**, 134426 (2002).
[20] R. Ferré, K. Ounadjela, J. M. George, L. Piraux, and S. Dubois, Phys. Rev. B **56**, 14066 (1997).
[21] T. G. Sorop, C. Untiedt, F. Luis, M. Kröll, M. Rasa, and L. J. de Jongh, Phys. Rev. B **67**, 014402 (2003).
[22] Q. F. Liu, J. B. Wang, Z. J. Yan, and D. S. Xue, Phys. Rev. B **72**, 144412 (2005).
[23] E. H. Frei, S. Shtrikman, and D. Treves, Phys. Rev. **106**, 446 (1957).
[24] A. Aharoni and S. Shtrikman, Phys. Rev. **109**, 1522 (1958).
[25] R. Skomski and J. M. D. Coey, *Permanent Magnetism* (Institute of Physics, Bristol, 1999).
[26] E. C. Stoner and E. P. Wohlfarth, Philos. Trans. R. Soc. London, Ser. A **240**, 599 (1948).
[27] W. Wernsdorfer, B. Doudin, D. Mailly, K. Hasselbach, A. Benoit, J. Meier, J.-Ph. Ansermet, and B. Barbara, Phys. Rev. Lett. **77**, 1873 (1996).
[28] F. Ono and H. Maeta, Physica B **161**, 134 (1989).
[29] G. Herzer, Mater. Sci. Eng., A **133**, 1 (1991).
[30] K. Soulantica, F. Wetz, J. Maynadié, A. Falqui, R. P. Tan, T. Blon, B. Chaudret, and M. Respaud, Appl. Phys. Lett. **95**, 152504 (2009).